FEM STUDY OF THERMOMECHANICAL WELDING OF AUSTENITIC STAINLESS STEEL AND EXPERIMENTAL VALIDATION

P. WANG*, B. SZALOWSKI*, J. E. AZUKE**, R. VALLANT*,
M. C. POLETTI*, N. ENZINGER*

**Institute of Materials Science, Joining and Forming, Graz University of Technology, Kopernikusgasse 24/I, 8010 Graz, Austria*
***Faculty of Engineering at the Mondragon University, Goiru Kalea, 2, 20500 Arrasate, Gipuzkoa, Spain*

DOI 10.3217/978-3-85125-968-1-10

ABSTRACT

A coarse-grained microstructure is usually formed in the fusion zone (FZ) and heat-affected zone (HAZ) of TIG welds. The coarse grains usually degrade the service performance and difficult the inspection of welds. Since the austenitic stainless steels do not transform in solid-state, hammering applied on the hot already solidified weld during cooling can be used to promote grain refinement. In this study, large local plastic deformation on the solidified TIG welds of AISI 304L austenitic stainless steel was applied by frequent hammering (at 35 Hz) at a distance of 20 mm behind the welding heat source. The microstructure of welds with and without hammering are characterized using light optical microscopy. Additionally, the temperature, effective strain, and effective strain rate distributions were calculated using the finite element modelling, simulating the integrated arc welding and frequently plastic deformation via the SFTC Deform®-3D. The microstructures were significantly refined in FZ due to mechanical vibration of the solidifying phase and dynamic recrystallization of the solid phase due to large local strains and strain rates. The grains in the HAZ remain coarse because of the negligible plastic deformation. The fusion line can be simulated accurately, and larger temperature heterogeneity was observed in the hammered welds. Therefore, the coupled thermomechanical simulation revealed the correlation of microstructure refinement in the weld and the thermomechanical welding process.

Keywords: Austenitic stainless steel; Thermomechanical welding; Mechanical vibration; Grain refinement; FEM simulation

INTRODUCTION

Fusion welding, as one of the most essential joining methods, is usually used for manufacturing austenitic stainless steels (ASS), for example the Tungsten Insert Gas (TIG) welding for AISI 304L [1, 2]. Although its simplicity of execution, TIG welding usually involves a large localized heat input, and the weld region experiences complex thermal cycles due to localized heating and cooling steps. Generally, these result in large residual stress and heterogeneous microstructures, as well as coarse-grains in the fusion zone (FZ) and heat-affected zone (HAZ) of the welds [3]. Grain size has a significant impact on material properties [2, 4]. Refining the weld microstructure can improve mechanical properties such as tensile strength, hardness, and toughness [4, 5]. Grain refinement methods include various heat treatment processes occurring after phase transformation or twining [1, 6], the application of mechanical and/or electromagnetic vibrations during welding or additive manufacturing [7-9], and the thermomechanical processing, for example involving severe plastic deformation [10]. Due to the absence of phase transformation in the ASS during the cooling stage when performing the fusion welding, grain refinement of weld microstructures can be achieved by utilizing vibration on the weld pool and plastic deformation on the solidifying weld. The finite element method (FEM) is the predictive tool to investigate coupled or uncoupled thermal and mechanical analysis of welding processes: temperature field, plastic deformation and heat source modelling [11, 12].

In this paper, the authors developed a 3D FE model of the proposed thermomechanical welding process, which can accurately predict the coupled thermomechanical fields (i.e., distributions of the effective strain, effective strain rate, and temperature), and also their corresponding evolution histories within both FZ and HAZ during the whole welding process.

RESEARCH METHOD

EXPERIMENTAL SETUP

The setup of the thermomechanical welding (TMW) system is presented in Fig. 1 (a) with a pneumatic hammer. The properties of the pneumatic hammer are the average free stroke of 13 mm and a cycling frequency of 35 Hz at a constant air pressure of 6 bar [13, 14]. The hammer is made of 42CrMo4 steel with a hardness of 550 HV 10. The rectangular tip is with dimensions of 15 × 2 mm. Fig. 1 (b) shows the deformed surface after the hammering. Fig. 1 (c) shows a simple 2D diagram of the TMW system with four parameters, i.e., a1 to a4, determining the positions of the hammer and torch with a needle. The distances of the hammer and torch needle to the substrate are denoted by a1 and a2, respectively. a3 is the offset between the hammer and the torch needle and determines the distance of starting the hammering after the TIG welding. a4 is the tilt angle of the torch or torch needle, influencing on both, the power density and the final geometry of the fusion zone. The torch combined with the needle was held at a fixed height. The pneumatic hammer moves in a vertical direction. The substrate was moved unidirectionally at a specific speed, depending on the welding speed.

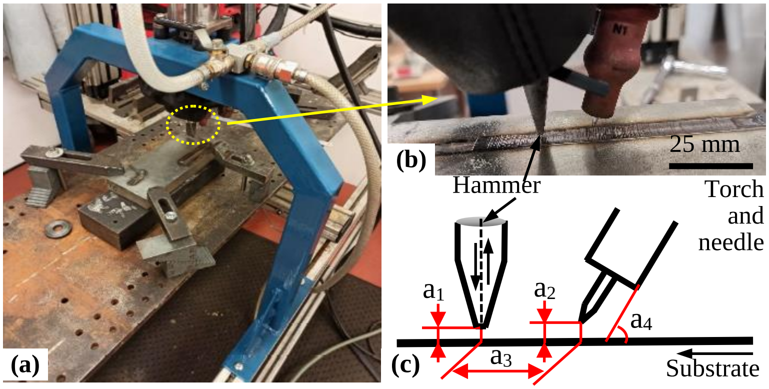

Fig. 1 (a) setup of the thermomechanical welding (TMW) system with a pneumatic hammer, (b) the magnified photo of the hammer and torch marked by the dashed ellipse in (a), and (c) a 2D schematic diagram of the TMW system with a1 to a4 showing the positions of hammer and torch

The cycling load of the hammer was measured by a load cell [13]. The temperature field adjacent to the TIG weld seam was determined by five individual K-type thermocouples aligned perpendicularly to the central line, and their positions (T1 to T5) are as shown in Fig. 2.

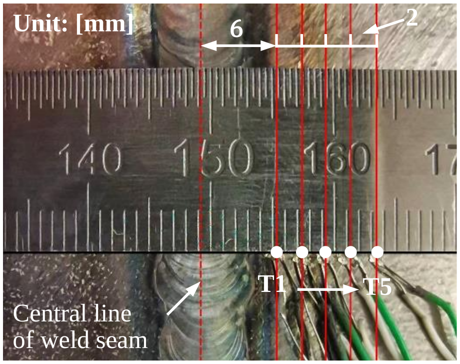

Fig. 2 Positions of the five K-type thermocouples T1 to T5 arranged away from the central line of the TIG bead plate weld seam

FE MODEL DESCRIPTION

Heat Source Model

The Goldak's double-ellipsoid heat source model was used to determine the distribution of the temperatures within the workpiece. The schematic illustration of Goldak's double ellipsoidal heat source model [15] is shown in Fig. 3. The parameters a_f and a_r are the lengths of front and rear semi-axes, and b and c are the width and depth of the heat source, respectively.

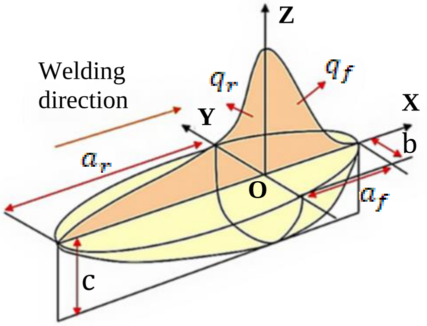

Fig. 3 Schematic diagram of the Goldak's double ellipsoidal heat source model [16]

The Goldak's double-ellipsoid heat source model can be described by two power densities, i.e., q_f in Eq. 1 and q_r in Eq. 2, belonging to the frontal and rear ellipsoids, respectively. The calibration of both Eq. 1 and Eq. 2 consists in adjusting the three parameters k, l, and m. In this way, the modified and calibrated double ellipsoidal heat source can be used for the TIG welding simulation via the Deform®-3D software. The parameters f_f and f_r are the factors for distributing the energy input power Q to the front and rear ellipsoids of heat source, where its sum equals two (Eq. 3). Considering the FZ geometry and the continuity of the volumetric heat source, the factor f_f is calculated according to Eq. 4 [17, 18]. The size of the fusion zone is determined by a_f, a_r, b and c. These four parameters are measured on the basis of carried out experiments and are taken from the cross-section metallography of the weld seam. The heat source properties are shown in Table 1.

$$q_f\left(x,y,z\right)=\frac{6\sqrt{3}Qf_f}{\pi\sqrt{\pi}a_f bc}\exp[-(\frac{kx^2}{a_f{}^2}+\frac{ly^2}{b^2}+\frac{mz^2}{c^2})] \tag{1}$$

$$q_r\left(x,y,z\right)=\frac{6\sqrt{3}Qf_r}{\pi\sqrt{\pi}a_r bc}\exp[-(\frac{kx^2}{a_r{}^2}+\frac{ly^2}{b^2}+\frac{mz^2}{c^2})] \tag{2}$$

$$f_f + f_r = 2 \tag{3}$$

$$f_f = 2/(1 + a_f / a_r) \tag{4}$$

where $q_f(x, y, z)$ – thermal flow density of the frontal ellipsoid [W·mm^{-3}]; $q_r(x, y, z)$ – thermal flow density of the rear ellipsoid [W·mm^{-3}]; a_f, a_r, b, c– parameters for describing the dimension of the volume of heat input [mm]; x, y, z – point's coordinates [mm]; f_f, f_r – constants influencing energy distribution [-]; k, l, m – parameters used for modifying and calibrating the heat source [-]; Q – the overall heat source power [W].

Table 1 Parameters of the Goldak's double ellipsoidal heat source

a_f [mm]	a_r [mm]	b [mm]	c [mm]	η [-]	Q [W]	f_f [-]	f_r [-]	k [-]	l [-]	m [-]
3.49	2.08	3.26	1.20	0.88	1540	0.75	1.25	3	1.44	3.5

The overall heat source power Q is calculated as a product of both, the voltage and the current (Eq. 5). This result also needs to be multiplied by the heat transfer efficiency η from the heat source to the material. For the TIG welding method, the η does not change so much, and according to standards, it has values between 0.86 and 0.88 [19]. The value of η is set to 0.88.

$$Q = \eta U I \tag{5}$$

where, Q – heat source power [W]; U – welding voltage [V]; I – welding current [A]; η – the efficiency of heat transfer [-].

Mesh and Dimensions

The commercial FE software SFTC Deform®-3D (version 12.0) is used for the thermomechanical welding simulations. The geometric size of the FEM model is shown in Fig. 4. The chosen dimensions for the substrate were 100 × 50 × 30 mm with a total of 8000 tetrahedral elements with a prior size ratio of 2. Small tetrahedral elements were additionally set using the function of "Mesh windows" in the region affected by the TMW, as shown in Fig. 4. The size ratio to outside elements is 0.05. Additionally, the SFTC Deform®-3D has the function of automatically remeshing controlled by given remeshing criteria and weighting factors. The hammer was set as the rigid top die. A total of 500 steps with a step size of 0.1s/step were used for the FEM simulation.

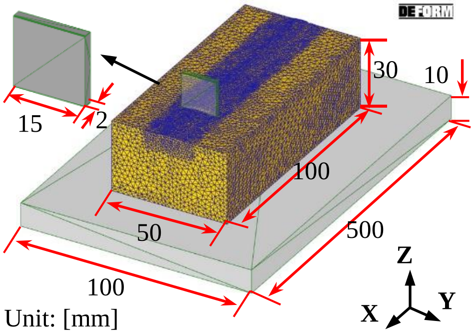

Fig. 4 Three-dimensional finite element mesh for the viscoplastic substrate and the rigid hammer in the thermomechanical welding system using the Deform®-3D model

Validation of the FE Model

Experimental validation was performed to prove the accuracy of the numerical simulation by the following aspects. The measured temperature curves of the five selected points (T1 ~ T5 seen in Fig. 2) adjacenssst to the weld seam were compared with the corresponding simulated values.

EXPERIMENTAL PROCEDURE

The TIG bead on plate welding and the TMW were both conducted on the identical substrate, i.e., an as-received hot-rolled AISI 304L plate with the dimensions of 100 × 50 × 30 mm. The composition of the investigated material is listed in Table 2. In addition, the heat capacity, the thermal conductivity coefficient, and the shear modulus can be found in Appendix 1, obtained from the software JMatPro$^{®}$-7.0. Their thermophysical properties were formally incorporated into the FE model (section 0) to optimize the material property.

Table 2 Chemical composition of the AISI 304L austenitic stainless steel (wt %)

Element	Cr	Mn	Ni	Si	C	N	P	S	Fe
Wt. %	18.055	1.773	8.010	0.374	0.018	0.071	0.036	0.001	Balance

The welding current and voltage were kept constant: 125 A and 14 V, respectively. The welding torch was fixed on a frame, and the relative moving speed of the plate was 2 mm/s. The offset between the hammer and torch was 20 mm. A constant air pressure (P_{air} [bar]) of 6 bar was used for the pneumatic hammer. The shield gas used was 100% Argon, with a flow rate of 12 1/s. All TMW parameters were listed in Table 3.

Table 3 Parameters of the thermomechanical welding

V [mm/s]	I [A]	U [V]	P_{air} [bar]	V_{Ar} [l/s]	a_1 [mm]	a_2 [mm]	a_3 [mm]	a_4 [°]
2	125	14	6	0.2	3	4	20	80

Standard metallographic techniques were used for cutting, grinding and polishing the samples at the cross-section of welds for microstructure analysis. The samples were electrolytically etched with a solution containing 60 vol% of nitric acid and 40 vol% distilled water [20, 21]. The microstructure was captured using a light optical microscope (Zeiss Observer.Z1m with an Axio-Cam-MRC5 camera). The contents of both phases were calculated via the ImageJ analyzer [21]. The movement of the hammer was controlled by adopting the "Mechanical press" type. The substrate and bottom die were both pushed to the +X direction at a constant speed of 2 mm/s.

RESULTS AND DISCUSSION

Fig. 5 (a) and (b) comparatively display the microstructures of the fusion zone in the single TIG weld and TMW weld, respectively. Coarse dendrites were observed in the TIG weld, and while fine solidified microstructure was obtained with the contribution of frequent hammering, as shown in Fig. 5 (b). The frequent plastic deformation and mechanical vibration [9, 23] were introduced to the weld during solidification, which resulted in the distinct solidification and grain growth modes. Apart from the large differences in the grain microstructure, the phase contents are different. Assuming that the black lines and dots in Fig. 5 are δ-ferrite and the rest is γ-austenite. The content of the vermicular δ-ferrite [24] in the TMW weld is 38.3 vol% , relatively higher than that in the TIG weld (22.4 vol%) and significantly higher than that in the initial condition (~ 3 vol% measured previously [25]).

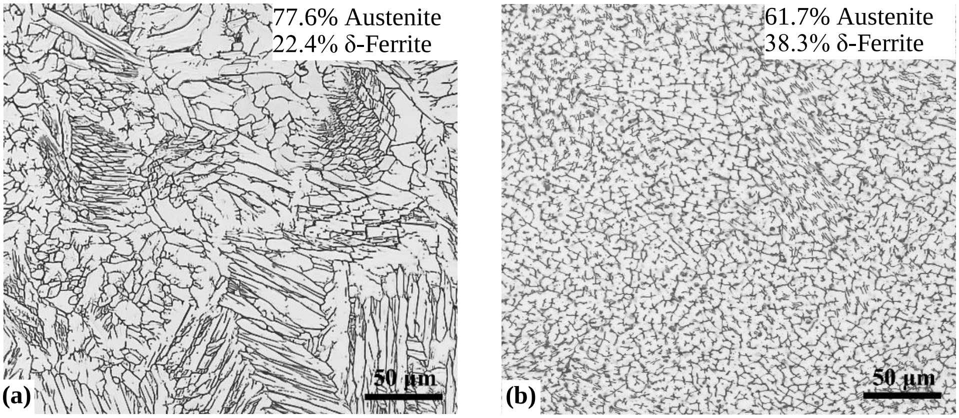

Fig. 5 LOM observations of the fusion zone in the TIG welding sample (a) and thermomechanical welding (i.e., TMW) sample (b) obtained at welding conditions of the current 125 A, speed 2 mm/s, and a 20 mm offset between the TIG torch and hammer for the TMW

In addition, the mirostructure of the HAZ for the TMW weld can be seen in Fig. 6. It shows that the grains in the HAZ is relatively larger than that of base material (BM) as a consequence of grain coarsening due to the large thermal effect [22].

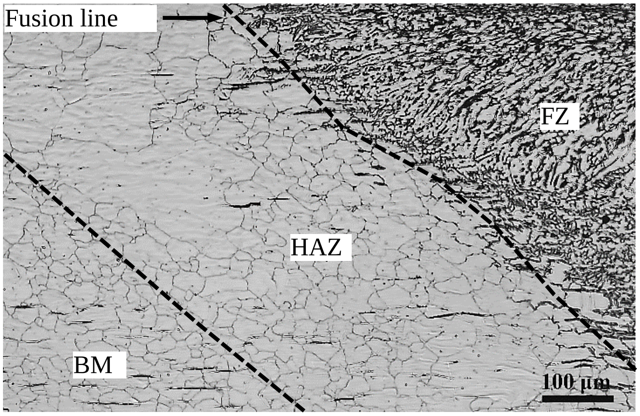

Fig. 6 LOM observation of the heat-affected zone at the cross-section of the thermomechanical welding (i.e., TMW) weld of AISI 304L austenitic stainless steel

Fig. 7 (a) shows the plots of simulated and measured temperature evolutions of the selected five points (i.e., T1 to T5, as shown in Fig. 2). The simulated data were obtained using the point tracking technique through the post-processing of Deform®-3D. It can be seen that a good fitness of these temperatures was obtained, which is identified by a higher determination coefficient (R^2 = 0.9925), evaluated from Fig. 7 (b) [26]. The optimized double ellipsoid heat source model with the adjusted model parameters *k*, *l*, *m*, and η in Eqs. (1 to 4), as well as the used temperature dependent materials properties can closely reproduce the real temperature fields.

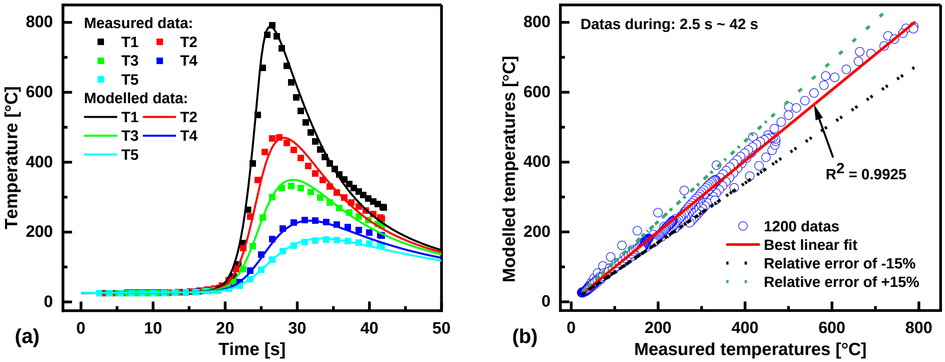

Fig. 7 Comparison of the simulated and measured temperature evolutions of points T1 to T5 from Fig. 2 using the point tracking technique (a), and the corresponding correlation evaluation of both data (b)

The temperature evolution at the FZ can be plotted at several specific points (D0 to D4) as shown in Fig. 8 (a). The point D0 is in the central line of the weld seam (i.e., the dash line as shown in Fig. 2), where the torch needle passed through. Points D1, D2, and D3 are located in the FZ, alinged perpendicularly to the welding trajectory and with 1 mm, 2 mm, and 3 mm distances away from the point D0, respectively. Due to the welding speed of 2 mm/s and the offset of 20 mm, the calculated time after the solidification and when the hammer hits the FZ is 10 s (between dashed lines) as shown in Fig. 8 (a). The temperatures of these four points are within the range of 440 °C ~ 465 °C, i.e., this should be the approximate temperature where the frequent hammering occurs afger the TIG welding conditions of current 125A and speed 2 mm/s. Fig. 8 (b) shows that the average hammering force is 5364 N measured by the load cell when the interspace of the hammer top tip to the substrate is 3 mm, i.e., the parameter a_1 as shown in Fig. 1 (c) equals to 3 mm.

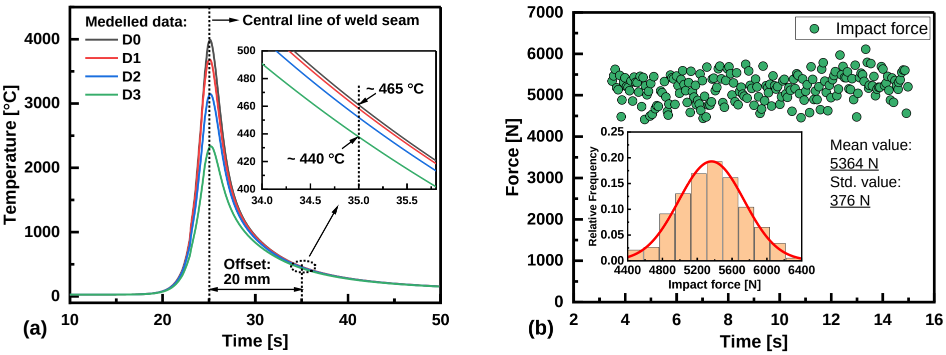

Fig. 8 Temperature evolution of four specific points in the TIG weld seam (D0 to D4) at welding conditions of current 125A and speed 2mms-1 (a), and (b) the evolution of maximum impact forces of frequent hammering measured by the load cell [13, 14]. D0 is located in the central line of the weld seam, and D1 ~ D3 is aligned with an interspace of 1 mm perpendicularly to the central line.

Fig. 9 shows the distribution maps of simulated effective strain, temperature, and effective strain rate on a slice, i.e., the cross-section of weld, and the corresponding histograms. The position of slice is where starting the hammering. It can be seen that the plastic deformation occurs generally in a small region, as indicated in Fig. 9 (a) and (c). Fig. 9 (b) displays the current temperatures that fit the temperature range as discussed in Fig. 8. In addition, the histograms of the effective strain, temperature, and effective strain rate are shown in Fig. 9 (d), (e) and (f), respectively. Such three histograms can be used for improving the processing parameters (for example, modifying hammer offsets to increase/decrease temperatures for starting deformation). In addition, the evolutions of the simulated temperature, effective strain, and effective strain rate of specific points in the TMW weld (i.e., FZ and HAZ) can be used to develop microstructure evolution models of the AISI 304L by incorporating the recrystallization models (SRX and DDRX) and grain coarsening.

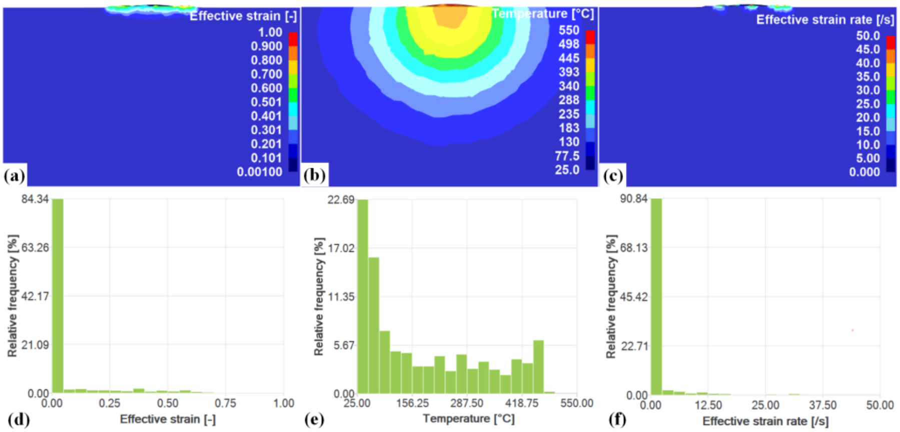

Fig. 9 Distributions of the effective strain (a), temperature (b), and effective strain rate (c) in a slice of the cross-section of AISI 304L thermomechanical weld at TIG welding conditions of current 125 A, voltage 14V, speed 2 mm/s, and a 20 mm offset between the TIG torch and hammer, and (d), (e) and (f) are the corresponding histograms of (a), (b) and (c), respectively

SUMMARY AND CONCLUSIONS

The TIG welding and thermomechanical welding (i.e., TMW) were both conducted on the samples of AISI 304L. TMW is composed of TIG welding and subsequent hammering. The plastic deformation was carried out on the cooling TIG weld using frequent hammering with a 20 mm offset between the TIG torch and hammer. The microstructures were compared to analyze the effect of frequent hammering on the microstructure evolution. With the aid of the finite element model, both fields and evolutions of temperature, effective strain, and effective strain rate on the TMW welds were modelled and experimentally validated. Several conclusions are summarized as follows,

a. The solidified microstructure of the fusion zone is relatively fine in the TMW weld than that in the TIG weld at conditions of welding current 125 A and welding speed 2 mm/s. The contribution of frequent hammering can promote the refinement of the fusion zone microstructure.
b. The finite element (FE) numerical results show that the simulated temperature field has a good agreement with the test measurements. The fields of simulated effective strain, effective strain rate, and temperature reveal the conditions of the deformation for the frequent hammering.
c. During the TMW process, the evolutions of temperature, effective strain, and effective strain rate can be obtained from the FEM simulation for selected points. These can be used in future steps for optimizing the TMW process and modelling the related microstructure evolution.

ACKNOWLEDGMENT

The authors carried out this work under the project of FWF Project in Austria-Thermomechanical welding (No. 16732).

APPENDIX I

Fig. A-1 shows the evolution curves of several simulated thermo-physical properties of the as-received AISI 304L, i.e., the thermal conductivity [W/(m·K)], the shear modulus *G* [GPa], and the specific heat coefficient C_p [J/(g·K)] with respect to temperature T [°C]. These data were simulated by the JMatPro®- v. 7.0 calculated with the compositions as listed in Table 2, which were used to adjust the temperature-dependent material properties in the Deform®-3D FEM model.

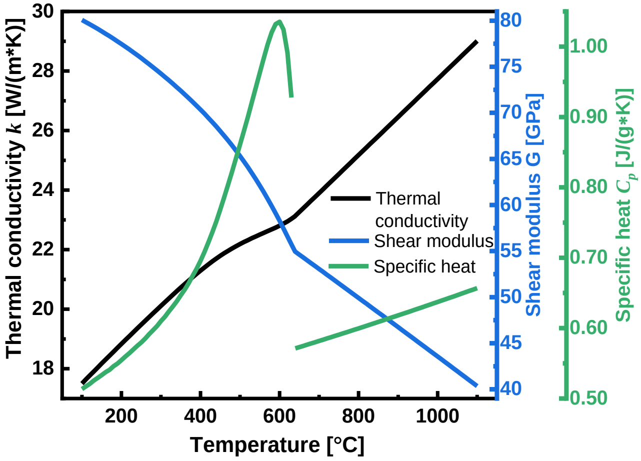

Fig. A-1 The simulated material properties of thermal conductivity, heat capacity, and shear modulus of the as-received AISI 304L by JMatPro®- v. 7.0

References

[1] F. SADEGHI ET AL.: ‘Role of the annealing twin boundary on the athermal alpha'-martensite formation in a 304 austenitic stainless steel’, *Materialia*, 20, 2021.

[2] L.C. LI ET AL.: ‘Effect of welding heat input on grain size and microstructure of 316L stainless steel welded Joint’, *Applied Mechanics and Materials*, Trans Tech Publ., 2013.

[3] P. VASANTHARAJA ET AL.: ‘Assessment of Residual Stresses and Distortion in Stainless Steel Weld Joints’, *Materials and Manufacturing Processes*, 27(12), p. 1376-1381, 2012.

[4] J. MORRIS JR: ‘The influence of grain size on the mechanical properties of steel’, 2001.

[5] P. WANG ET AL.: ‘Effect of grain ultra-refinement on microstructure, tensile property, and corrosion behavior of low alloy steel’, *Materials Characterization*, 179, p. 111385, 2021.

[6] D. PODDAR, A. CHAKRABORTY and RAVI KUMAR B.: ‘Annealing twin evolution in the grain-growth stagnant austenitic stainless steel microstructure’, *Materials Characterization*, 155, p. 109791, 2019.

[7] T. WEN ET AL.: ‘Influence of high frequency vibration on microstructure and mechanical properties of TIG welding joints of AZ31 magnesium alloy’, *Transactions of Nonferrous Metals Society of China*, 25(2), p. 397-404, 2015.

[8] M. SABZI and S.M. DEZFULI: ‘Drastic improvement in mechanical properties and weldability of 316L stainless steel weld joints by using electromagnetic vibration during GTAW process’, *Journal of Manufacturing Processes*, 33, p. 74-85, 2018.

[9] C. MA ET AL.: ‘Investigation of In Situ Vibration During Wire and Arc Additive Manufacturing’, *3d Printing and Additive Manufacturing*, 2021.

[10] S.M. AL-QAWABAH and A.I. ZAID: ‘Different methods for grain refinement of materials’, *International Journal Of Scientific & Engineering Research*, Volume 7, Issue 7, p. 8, 2016.

[11] A.K. MONDAL ET AL.: ‘Development of avocado shape heat source model for finite element based heat transfer analysis of high-velocity arc welding process’, *International Journal of Thermal Sciences*, 166, p. 107005, 2021.

[12] J.J. XU ET AL.: ‘Temperature and residual stress simulations of the NeT single-bead-on-plate specimen using SYSWELD’, *International Journal of Pressure Vessels and Piping*, 99-100, p. 51-60, 2012.

[13] J.E. AZKUE: *In-situ analysis of thermomechanical welding process*, bachelor thesis Mondragon University Faculty of Engineering, Spain, 2022.

[14] B. SZAŁOWSKI ET AL.: ‘Effect of local deformation during TIG welding of austenitic stainless steel on the microstructure and hardness’, in *ESSC & Duplex 2022*, Verona, Italy, 2022.

[15] J. GOLDAK, A. CHAKRAVARTI and M. BIBBY: ‘A new finite element model for welding heat sources’, *Metallurgical Transactions B*, 15(2), p. 299-305, 1984.

[16] Z. SAMAD, N.H.M. NOR and E.R.I. FAUZI: ‘Thermo-Mechanical Simulation of Temperature Distribution and Prediction of Heat-Affected Zone Size in MIG Welding Process on Aluminium Alloy EN AW 6082-T6’, *IOP Conference Series: Materials Science and Engineering*, 530, 2019.

[17] G. FU ET AL.: ‘Parameter determination of double-ellipsoidal heat source model and its application in the multi-pass welding process’, *Ships and Offshore Structures*, 10(2), p. 204-217, 2015.

[18] A. LUNDBÄCK: *Finite element modelling and simulation of welding of aerospace components*, thesis, Luleå tekniska universitet, 2003.

[19] J. DUPONT and A. MARDER: ‘Thermal efficiency of arc welding processes’, *Welding Journal-Including Welding Research Supplement*, 74(12), p. 406s, 1995.

[20] B. SZAŁOWSKI: *Effect of Thermomechanical Welding on the Austenitic Stainless Steel*, master thesis, Institute of Materials Science, Joining and Forming, Graz University of Technology, 2022.

[21] A. BAGHDADCHI, V.A. HOSSEINI and L. KARLSSON: ‘Identification and quantification of martensite in ferritic-austenitic stainless steels and welds’, *Journal of Materials Research and Technology-Jmr&T*, 15, p. 3610-3621, 2021.

[22] T. SAKAI ET AL.: ‘Dynamic and post-dynamic recrystallization under hot, cold and severe plastic deformation conditions’, *Progress in Materials Science*, 60, p. 130-207, 2014.

[23] H.H. ZARGARI ET AL.: ‘Metallurgical Characterization of Penetration Shape Change in Workpiece Vibration-Assisted Tandem-Pulsed Gas Metal Arc Welding’, *Materials*, 13(14), 2020.

[24] S.A. DAVID: ‘Ferrite Morphology and Variations in Ferrite Content in Austenitic Stainless-Steel Welds’, *Welding Journal*, 60(4), p. S63-S71, 1981.

[25] M.F. SIDDIQUI: *Recrystallization and Grain Growth Behavior of Austenitic Stainless Steel 304L*, master thesis, IMAT-Institute of Materials Science, Joining and Forming, Graz University of Technology, 2021.

[26] D. SAMANTARAY, S. MANDAL and A.K. BHADURI: ‘A critical comparison of various data processing methods in simple uni-axial compression testing’, *Materials & Design*, 32(5), p. 2797-2802, 2011.